Draft version May 11, 2022
Typeset using LaTeX **twocolumn** style in AASTeX631

arXiv:2205.04742v1 [astro-ph.GA] 10 May 2022

Cloudlet Capture Model for Asymmetric Molecular Emission Lines Observed in TMC-1A with ALMA

Tomoyuki Hanawa,[1] Nami Sakai,[2] and Satoshi Yamamoto[3]

[1] *Center for Frontier Science, Chiba University, 1-33 Yayoi-cho, Inage-ku, Chiba 263-8522, Japan*
[2] *RIKEN Cluster for Pioneering Research, 2-1 Hirosawa, Wako-shi, Saitama 351-0198, Japan*
[3] *Department of Physics, The University of Tokyo, Bunkyo-ku, Tokyo 113-0033, Japan*

(Received December 10, 2021; Revised March 28, 2022; April 27, 2022; Accepted May 6, 2022)

Submitted to ApJ

ABSTRACT

TMC-1A is a protostellar source harboring a young protostar, IRAS 04365+2353, and shows a highly asymmetric features of a few 100 au scale in the molecular emission lines. Blue-shifted emission is much stronger in the CS (J = 5-4) line than red-shifted one. The asymmetry can be explained if the gas accretion is episodic and takes the form of cloudlet capture, given the cloudlet approached toward us. The gravity of the protostar transforms the cloudlet into a stream and changes its velocity along the flow. The emission from the cloudlet should be blue-shifted before the periastron, while it should be red-shifted after the periastron. If a major part of cloudlet has not reached the periastron, the former should be dominant. We perform hydrodynamical simulations to examine the validity of the scenario. Our numerical simulations can reproduce the observed asymmetry if the orbit of the cloudlet is inclined to the disk plane. The inclination can explain the slow infall velocity observed in the $C^{18}O$ (J=2-1) line emission. Such episodic accretion may occur in various protostellar cores since actual clouds could have inhomogeneous density distribution. We also discuss the implication of the cloudlet capture on observations of related objects.

Keywords: Young stellar objects – Interstellar medium – Interstellar molecules – Protostars – Star formation

1. INTRODUCTION

Young Stellar objects often show signatures of rotating disks and their formation is an integral part of star formation. The disks are roughly symmetric around the rotation axis, though some of them have spirals and other substructures (see, e.g., Andrews et al. 2018; Sakai et al. 2019; Nakatani et al. 2020). Thus, we often assume implicitly that they are almost symmetric from the birth. However, some young objects show highly asymmetric features according to high-resolution molecular line observations with ALMA (see, e.g., Yen et al. 2014; Sakai et al. 2016; Pineda et al. 2020; Artur de la Villarmois et al. 2019, for L1489, TMC-1A, Per-emb2 and GSS30-IRS5, respectively), even though are not close binaries. In addition, non-axisymmetric distribution of the infalling gas around the protostar is often suggested from the asymmetry of spectral line profiles, although it is spatially unresolved (e.g., L483 and B335 Oya et al. 2017; Imai et al. 2019, respectively). More recently, Garufi et al. (2022) have reported streamers in DG Tau and HL Tau. Even for the Class II source GM Aur, the asymmetric infall of the gas of a remnant envelope or a cloud component has been reported (Huang et al. 2021).

Star forming gas clouds are turbulent and inhomogeneous (see, e.g., the review by Hennebelle and Falgarone 2012). Hence, the gas accretion onto young stellar objects can be variable on a short timescale, though the accretion rate is thought to decrease along the evolution (Küffmeier et al. 2017). Based on the above recognition, Dullemond et al. (2019) have proposed that the gas accretion is sporadic in the late stage of star formation and some Class II objects have secondary disks formed by the capture of a cloudlet (see also Küffimeier et al.

Corresponding author: Tomoyuki Hanawa
hanawa@faculty.chiba-u.jp

2019). More recently, Küffmeier et al. (2021) have made numerical simulations in which the captured cloud forms an outer disk surrounding a pre-existing inner disk.

The argument by Dullemond et al. (2019) is supported by the large arc-like feature observed in some sources such as AB Aur (see, e.g., Fukagawa et al. 2004). Their hydrodynamical simulations reproduce the arc-like feature. Their model is an interesting idea to be examined further, though the arc-like feature may be produced by another mechanism such as Rossby wave instability (see, e.g., Miranda et al. 2016).

Capture of a cloudlet may take place in an earlier stage of star formation. A few years earlier than Dullemond et al. (2019), the asymmetric molecular distribution is reported in the prestellar source, TMC-1A (Sakai et al. 2016). TMC-1A, which harbors the Class I protostar IRAS 04365+2535, is a typical example showing such asymmetry in the molecular emission lines (see, e.g., Sakai et al. 2016; Bjerkelli et al. 2016; Harsono et al. 2021) and shows clear blue-red asymmetry in the molecular emission lines. Blue-shifted emission in the East part is much stronger than red-shifted one in the West. The morphology and degree of asymmetry depend on the chemical species emitting lines. The highly asymmetric morphology is unlikely to be ascribed to different chemical composition or excitation condition. This asymmetry may be short lived, since rotation around the protostar should reduce the asymmetry on the local Keplerian timescale.

In order to explain observed features of TMC-1A, Sakai et al. (2016) introduced a ballistic model, in which only the gravity of the protostar is assumed to act on an accreting gas element. We aim to reexamine this picture by using hydrodynamic simulations in which we take account of the collision of the infalling gas with the disk. Another issue of TMC-1A is the mass of the protostar. It is highly uncertain and ranges from 0.25 $M_\odot$ to 0.7 $M_\odot$ (Aso et al. 2015; Bjerkelli et al. 2016; Sakai et al. 2016). This uncertainty is in part due to the difference in the molecular emission lines used for the mass estimate. We should remember that the derived mass depends on the inclination of the gas motion to the line of sight. The current estimate is based on the assumption that the gas flow is confined in the disk plane. This assumption may be invalid.

Our numerical simulations are similar to those of Dullemond et al. (2019); Küffimeier et al. (2019); Küffmeier et al. (2021) but updated in some respects. First, we take account of the presence of a rotating disk around the protostar and its dynamical interaction with the infalling gas. Second, we take account of warm gas surrounding the disk and protostar. The cloudlet and disk gas are cold and dense while the pressure is the same as that of the surrounding warm gas. The temperature is assumed to remain nearly constant at a few tens Kelvin and several hundreds Kelvin in the cold and warm gases, respectively. The pressure of the warm gas prevents the dispersal of a cloudlet seen in the isothermal model of Küffimeier et al. (2019). Our model is similar to their adiabatic model but the specific heat ratio is assumed to be $\gamma = 1.05$. This low specific heat ratio mimics the short thermal timescale. The temperature of the gas increases temporally through kinetic energy dissipation by shock but goes back to its initial one on a timescale much shorter than the dynamical timescale. The gas temperature increases little in our model since it is proportional $T \propto \rho^{\gamma-1}$.

Our hydrodynamic model can reproduce the blue-asymmetry of the CS emission observed in TMC-1A under the assumption that the CS molecules are contained only in the cloudlet. This assumption is reasonable since the CS molecules are often abundant in an infalling-rotating envelope but not in disks (Sakai et al. 2014b). It can explain also the shift of SO emission peak to the disk center (Sakai et al. 2016). Furthermore, it can explain slow infall velocity observed in the $C^{18}O$ emission line (Aso et al. 2021) if the orbital plane of the cloudlet is nearly face-on.

This paper is organized as follows. We describe our model and numerical methods in §2, and results in §3. We compare our models with the observations in §4 and discuss implications in §5.

2. MODEL

2.1. *Basic Equations*

We solve the hydrodynamic equations on the cylindrical coordinates according Hanawa & Matsumoto (2021). They have succeeded in conservation of the the z-component of the angular momentum and the free stream preservation. The latter guarantees that it can solve a uniform flow without truncation errors. See Hanawa & Matsumoto (2021) for more technical details including numerical tests.

We use the hydrodynamical equations,

$$\frac{\partial \rho}{\partial t} + \nabla (\rho \mathbf{v}) = 0, \tag{1}$$

$$\frac{\partial}{\partial t} (\rho \mathbf{v}) + \nabla (\rho \mathbf{v}\mathbf{v} + P\mathbf{I}) = -\rho \nabla \Phi, \tag{2}$$

to describe gas accretion onto a protostar associated with a gas disk. The symbols, ρ and P, denote the density and pressure, respectively, while $\mathbf{v}$ and Φ do the velocity and gravitational potential, respectively. The

gas pressure is expressed as

$$P = \frac{k}{\bar{m}} \rho T, \tag{3}$$

where T, k, and $\bar{m}$ denote the temperature, Boltzmann constant, and mean molecular weight, respectively.

We assume that the gas consists of cold and warm components. The disk and cloudlet are composed of the cold molecular gas, while they are surrounded by a warm atomic gas. We assume the mean molecular weight to be 2.3 $m_{\rm H}$ and 1.27 $m_{\rm H}$ for the cold and warm gases, respectively, where $m_{\rm H}$ denotes the mass of a hydrogen atom. The assumed mean molecular weight means that the cloud gas is molecular while the warm gas is atomic and neutral. Both the cold and warm gases maintain their temperatures since their thermal timescales are much shorter than the dynamical one. In order to mimic the nearly isothermal change, we assume that the the gas is adiabatic with the specific heat ratio, $\gamma = 1.05$. Then we can use the energy conservation

$$\frac{\partial}{\partial t}(\rho E) + \nabla \cdot [(\rho E + P)\,\mathbf{v}] = -\rho \mathbf{v} \cdot \nabla \Phi, \tag{4}$$

$$E = \frac{\mathbf{v} \cdot \mathbf{v}}{2} + \frac{P}{(\gamma - 1)\,\rho}, \tag{5}$$

to follow the change in the pressure.

We introduce a color field,

$$c = \begin{cases} 1 & \text{(cloudlet)} \\ 0 & \text{(warm gas)} \\ -1 & \text{(gas disk)} \end{cases}. \tag{6}$$

to trace the cloudlet and gas disk. The color (scalar) field is traced by

$$\frac{\partial}{\partial t}(c\rho) + \nabla \cdot (c\rho \mathbf{v}) = 0. \tag{7}$$

We use the cylindrical coordinates, (r, φ, z), in our computation. We locate the protostar at the origin, $r = z = 0$. We also use the Cartesian coordinates, $(x, y, z) = (r\cos\varphi, r\sin\varphi, z)$ in our presentation. For simplicity, we ignore the self-gravity of the gas. This simplification is justified since we consider a cloudlet of $\lesssim 10^{-4}$ $M_\odot$ and gas disk of $< 10^{-2}$ $M_\odot$. Then the gravitational potential is expressed as

$$\Phi = \begin{cases} -\dfrac{GM}{\sqrt{r^2 + z^2}} & (r^2 + z^2 \geq a^2) \\ -\dfrac{GM}{2a^3}\left(3a^2 - r^2 - z^2\right) & (r^2 + z^2 < a^2) \end{cases}, \tag{8}$$

where M and a denote the mass of the protostar and the length scale, respectively. The mass of the protostar is uncertain and different values are adopted in the literature (0.68. 0.4, and 0.25 M$\odot$ in Aso et al. 2015; Bjerkelli et al. 2016; Sakai et al. 2016, respectively). In this paper we adopt an intermediate value of $M = 0.53$ $M_\odot$. The velocity and timescale given in this paper are proportional to the square root of the mass ($\propto M^{1/2}$, while the temperature is proportional to the mass ($\propto M$). We take the length scale to be $a = 50$ au to avoid numerical difficulties due to strong gravity in the region of $r \leq 50$ au.

We solve Equations (1), (2), (4), and (7) simultaneously in our simulations. We do not take account of magnetic fields, radiation processes, and turbulence for simplicity.

2.2. *Initial Model*

We assume that the warm gas is static and in an isothermal hydrostatic equilibrium.

$$P = P_0 \exp\left(-\frac{\bar{m}_0 \Phi}{kT_0}\right), \tag{9}$$

where P_0, T_0, and $\bar{m}_0$ denote the pressure in the region very far from the star, the initial temperature, and the mean molecular weight, respectively. The pressure is set to be $P_0 = 1.56 \times 10^7$ K cm^{-3} in this paper, though it can be set scale-free. The solution is still valid if we multiply both the density and pressure by the same arbitrary constant. The hydrogen is assumed to be in the atomic form in the warm gas and its mean molecular weight is evaluated to be $\bar{m}_0 = 1.27$ $m_{\rm H}$, where $m_{\rm H}$ denotes the mass of a hydrogen atom. Accordingly, the density is expressed as

$$\rho = \frac{\bar{m}_0 P_0}{kT_0} \exp\left(-\frac{\bar{m}_0 \Phi}{kT_0}\right). \tag{10}$$

We consider the density distribution where the density at $r = a$ is enhanced from that at infinity by a factor $e^{5/3} = 5.29$, i.e., $kT_0 = (3/5)GM\bar{m}_0/a$. This means that the assumed temperature is $T_0 = 883$ K. This temperature may be slightly higher than the real value, though it is highly uncertain (see, e.g., Figure 1 of Dutrey et al. 2014).

If the temperature is lower, the warm gas is more concentrated around the protostar but will not affect the result significantly because the cloudlet is also compressed to have a higher density around the protostar.

Next, we consider a gas disk rotating around the protostar. The disk is assumed to be stationary and axially symmetric. The rotation velocity is expressed as

$$\mathbf{v} = \begin{cases} v_\varphi(r)\mathbf{e}_\varphi & |z| < z_s(r) \\ 0 & |z| \geq z_s(r) \end{cases}, \tag{11}$$

where $z_s(r)$ and $\mathbf{e}_\varphi$ denote the half thickness of the disk and the unit vector in the φ-direction, respectively. Then the equation of motion reduces to

$$-\frac{{v_\varphi}^2}{r}+\frac{1}{\rho}\frac{\partial P}{\partial r}+\frac{\partial \Phi}{\partial r}=0, \tag{12}$$

$$\frac{1}{\rho}\frac{\partial P}{\partial z}+\frac{\partial \Phi}{\partial z}=0. \tag{13}$$

We assume that the temperature is uniform at $T=T_{\rm d}$ inside the disk ($|z|<z_s(r)$), while it is at $T=T_0$ outside the disk. Then the solutions of Equations (12) and (13) are expressed as

$$\rho(r,z)=\frac{\bar{m}_{\rm d}}{kT}P(r,z), \tag{14}$$

$$P(r,z)=P_s(r)\exp\left\{-\frac{\bar{m}_{\rm d}[\Phi(r,z)-\Phi(r,z_s)]}{kT_{\rm d}}\right\}, \tag{15}$$

$$P_s(r)=P_0\exp\left[-\frac{\bar{m}_0\Phi(r,z_s)}{kT_0}\right]. \tag{16}$$

$$v_\varphi^2=r\left(1-\frac{\bar{m}_0 T_{\rm d}}{\bar{m}_{\rm d}T_0}\right)\left(\frac{\partial \Phi_s}{\partial r}+\frac{dz_s}{dr}\frac{\partial \Phi_s}{\partial z}\right), \tag{17}$$

where $\bar{m}_{\rm d}$ denotes the mean molecular weight of the disk gas and is assumed to be $\bar{m}_{\rm d}=2.3\ m_{\rm H}$. Note that this model accomplishes the pressure balance on the disk surface.

We assume that the disk has the initial radius, $r_{\rm d}$, and the half thickness,

$$z_s=\beta\sqrt{{r_{\rm d}}^2-r^2}, \tag{18}$$

where β is a non-dimensional free parameter and taken to be 0.2 in this paper. This model can not reproduce flaring of the outer disk, because the spatial resolution is limited. This simple model is more durable against numerical instability than more realistic one due to stability against hydrodynamic waves.

We assume that a cloudlet occupies a spherical region,

$$(x-x_{\rm c})^2+(y-y_{\rm c})^2+(z-z_{\rm c})^2\le {a_{\rm c}}^2, \tag{19}$$

$$\mathbf{r}_c=\begin{pmatrix}x_{\rm c}\\ y_{\rm c}\\ z_{\rm c}\end{pmatrix}=\begin{pmatrix}r_{\rm c}\cos\psi_{\rm c}\\ 0\\ r_{\rm c}\sin\psi_{\rm c}\end{pmatrix}, \tag{20}$$

at the initial stage, where $r_{\rm c}$, $a_{\rm c}$, and $\psi_{\rm c}$ denote the distance to the cloud center, the cloudlet radius, and the inclination of the orbit of the cloudlet to the disk, respectively. The initial pressure inside the cloudlet is the same as given by Equation (9). We assume that the cloudlet has the initial temperature, $T_{\rm c}$, and the mean molecular weight, $\bar{m}_{\rm c}=2.3\ m_{\rm H}$. Then, the density is expressed as

$$\rho=\frac{\bar{m}_c P_0}{kT_c}\exp\left(-\frac{\bar{m}_0\Phi}{kT_0}\right). \tag{21}$$

The initial velocity is uniform at

$$\mathbf{v}_{\rm c}=\begin{pmatrix}v_{c,x}\\ v_{c,y}\\ v_{c,z}\end{pmatrix}=\begin{pmatrix}-\cos\psi_{\rm c}\sqrt{\dfrac{2GM}{r_{\rm c}}-\dfrac{2GM}{r_{\rm min}}}\\ \dfrac{\sqrt{2GMr_{\rm min}}}{r_{\rm c}}\\ -\sin\psi_{\rm c}\sqrt{\dfrac{2GM}{r_{\rm c}}-\dfrac{2GM}{r_{\rm min}}}\end{pmatrix} \tag{22}$$

inside the cloudlet. This initial velocity coincides with the velocity of a particle having a parabolic orbit with the periastron, $r_{\rm min}$, at the distance $r_{\rm c}$. The parabolic orbit lies in the xz plane and is inclined by ψ_c from the z-axis.

The temperature is assumed to be $T_{\rm c}=0.015GM\bar{m}_c/ka$ in the cloudlet and $T_{\rm d}=0.03GM\bar{m}_d/ka$ in the disk. Accordingly it is $T_{\rm c}=39$ K in the cloudlet and $T_{\rm d}=78$ K in the disk, for $M=0.53\ {\rm M}_\odot$ and $\bar{m}_{\rm c}=\bar{m}_{\rm d}=2.3m_{\rm H}$.

The numerical grid is designed so that the radial spatial resolution is constant at $\Delta r=1$ au and each numerical cell is almost isotropic, $r\Delta\varphi\simeq\Delta r$, in the inner region of $r\le 64$ au. In the outer region of $r>64$ au, the angular resolution is constant at $\Delta\varphi=0.938^\circ$ and the radial spatial resolution is $\Delta r=1.56\times10^{-2}r$. The vertical spatial resolution is $\Delta z=1$ au in near the mid plane ($|z|<64.5$ au and $\Delta z=1.56\times10^{-2}|z|$ in the outer regions of $|z|>64.5$ au. The numerical cell covers the cylindrical region of $r_{\rm out}$ and $|z|<z_{\rm out}$.

Table 1 summarizes the models shown in the following sections. The cloudlet is 500 au away from the central star at the initial stage except for in model A′. The orbit of the cloudlet is coplanar to the disk in models A, A′, and D, while it is inclined by 30° in models B and C.

Table 1. Model Parameters

model	$r_{\rm out}$ [a]	$z_{\rm out}$ [b]	$r_{\rm c}$ [c]	$a_{\rm c}$ [d]	$\psi_{\rm c}$ [e]
A	624 au	246 au	500 au	100 au	0°
A′	1254 au	246 au	1000 au	100 au	0°
B	624 au	392 au	500 au	100 au	30°
C	775 au	535 au	500 au	200 au	30°
D	775 au	336 au	500 au	200 au	0°

[a] The outer radius of the computation domain.
[b] The half height of the computation domain.
[c] The initial radial distance of the cloudlet.
[d] The initial radius of the cloudlet.
[e] The inclination of the cloudlet orbital plane to the disk plane. See Equation (20) for more details.

2.3. *Mock Observation*

We evaluate the emission expected from our numerical simulations as a post process for comparison with molecular line emission observed. We assume that our line of sight is parallel to

$$\mathbf{n}_3 = \begin{pmatrix} \sin\theta_{\rm obs}\cos\varphi_{\rm obs} \\ \sin\theta_{\rm obs}\sin\varphi_{\rm obs} \\ \cos\theta_{\rm obs} \end{pmatrix}, \tag{23}$$

where $\theta_{\rm obs}$ and $\varphi_{\rm obs}$ specify the location of the observer in the spherical coordinates. The disk inclination angle is given by $i = 180^\circ - \theta_{\rm obs}$. The radial velocity is evaluated to be $V = \mathbf{v}\cdot\mathbf{n}_3$ while the observer is located in the direction of $-\mathbf{n}_3$. Using the unit vectors,

$$\mathbf{n}_1 = \begin{pmatrix} \sin\chi_{\rm obs}\sin\varphi_{\rm obs} - \cos\chi_{\rm obs}\cos\theta_{\rm obs}\cos\varphi_{\rm obs} \\ -\sin\chi_{\rm obs}\cos\varphi_{\rm obs} - \cos\chi_{\rm obs}\cos\theta_{\rm obs}\sin\varphi_{\rm obs} \\ \cos\chi_{\rm obs}\sin\theta_{\rm obs} \end{pmatrix}, \tag{24}$$

$$\mathbf{n}_2 = \begin{pmatrix} -\cos\chi_{\rm obs}\sin\varphi_{\rm obs} - \sin\chi_{\rm obs}\cos\theta_{\rm obs}\cos\varphi_{\rm obs} \\ \cos\chi_{\rm obs}\sin\varphi_{\rm obs} - \sin\chi_{\rm obs}\cos\theta\sin\varphi_{\rm obs} \\ -\cos\chi_{\rm obs}\sin\theta_{\rm obs} \end{pmatrix}, \tag{25}$$

where $\chi_{\rm obs}$ denotes the disk position angle on the sky. We define the position angle so that it increases counterclockwise from the North. Then, we can define the Cartesian coordinates,

$$\mathbf{r} = X\mathbf{n}_1 + Y\mathbf{n}_2 + s\mathbf{n}_3, \tag{26}$$

where X and Y denote the projected distance from the protostar to the West and that to the North, respectively.

Our evaluation is based on the the simple assumption that the opacity at the line center is the same in the whole region. In other words, we ignore possible variation in the excitation temperature and abundance. Then, the optical depth is evaluated to be

$$\tau(X,Y,V) = \kappa_0\Sigma(X,Y,V), \tag{27}$$

$$\Sigma(X,Y,V) = \int_{c>0} \frac{c(\mathbf{r})\rho(\mathbf{r})}{\sqrt{2\pi}\sigma} \exp\left\{-\left[\frac{\mathbf{v}(\mathbf{r})\cdot\mathbf{n}_3 - V}{2\sigma^2}\right]^2\right\} ds, \tag{28}$$

$$\mathbf{r} = X\mathbf{n}_1 + Y\mathbf{n}_2 + s\mathbf{n}_3, \tag{29}$$

where V, κ_0, and σ denote the radial velocity, the opacity at the line center, and velocity dispersion, respectively. We assume $\sigma = 0.153$ km s^{-1} to be slightly smaller than the velocity resolution of the observation (0.4 km s^{-1}) so that we obtain smooth channel maps. The intensity is evaluated to be

$$I(X,Y,V) = I_0\{1 - \exp[-\tau(X,Y,V)]\}, \tag{30}$$

where I_0 denotes the intensity at the saturation level and should coincide with the Planck function at the excitation temperature of the line emitting molecule. When the line is optically thin, Equation (30) reduces to

$$I(X,Y,V) = I_0\kappa_0\Sigma(X,Y,V). \tag{31}$$

Thus, we compare the column density per unit velocity, $\Sigma(X,Y,V)$, with the observed intensity, since our numerical model cannot evaluate the opacity and excitation temperature quantitatively. The integrated intensity should be proportional to the column density along the line of sight as far as the line is optically thin and the temperature is uniform. We should evaluate the parameters, κ_0, σ, and I_0 from the abundance and excitation temperature for each transition. However we do not take account of the physical processes in our numerical simulation and hence the derived temperature is not accurate enough. In this paper, we assume $\sigma = 0.153$ km s^{-1} and take other constants arbitrarily.

3. RESULTS

3.1. *Model A*

First we examine a prototypical model named A, in which the cloudlet has the radius, $a_{\rm c} = 100$ au and is located at $r_{\rm c} = 500$ au at the initial stage, $t = 0$ yr. The mass and average density of the cloudlet are $M_{\rm cl} = 1.27\times10^{-5}$ M$_\odot$ and $\bar{\rho}_{\rm cl} = 1.80\times10^{-18}$ g cm^{-3}, respectively. The latter corresponds to the average number density, $\bar{n}_{\rm c;} = 4.73\times10^5$ cm^{-3}. The initial velocity of the cloudlet is 1.37 km s^{-1}. The disk half thickness is set to be 20 au ($\beta = 0.2$).

Figure 1 shows the initial stage, $t = 0$, and an early stage of the collision of the cloudlet with the disk, $t = 1498$ yr. The head of the cloudlet touches the disk edge at $t = 1130$ yr. The color denotes the density on the planes $x = 0$, $y = 0$, and $z = 0$ in each panel. The distribution of the cold gas is also shown by the volume rendering. The color scale on the top of each panel is for the cross sections, although a similar color scale is used for the volume rendering. The cloudlet shaves an outer part of the disk by the ram pressure. When colliding, the density is a little higher in the disk than in the cloudlet. Still, the ram pressure exceeds the disk gas pressure since the infall velocity is much higher than the sound speed.

Figure 2 denotes the deformation of the cloudlet in the period, $t \le 1800$ yr. Each curve denotes the surface

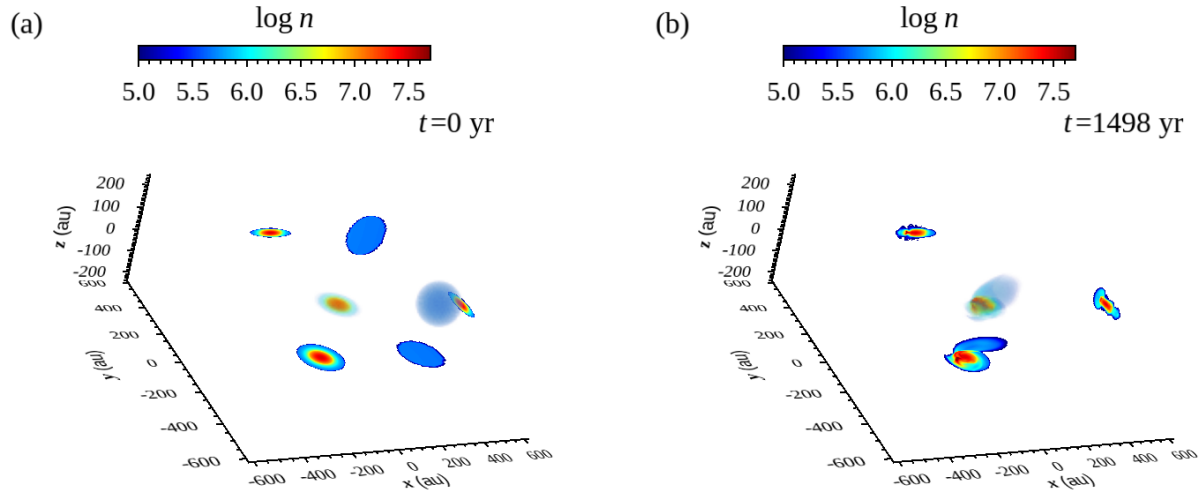


Figure 1. Panels a and b show the initial state ($t = 0$) and the stage at $t = 1.498 \times 10^3$ yr, respectively by combination of the volume rendering and the cross sections. A spherical cloudlet is located at a distance of 500 au from the star and disk at the initial stage.

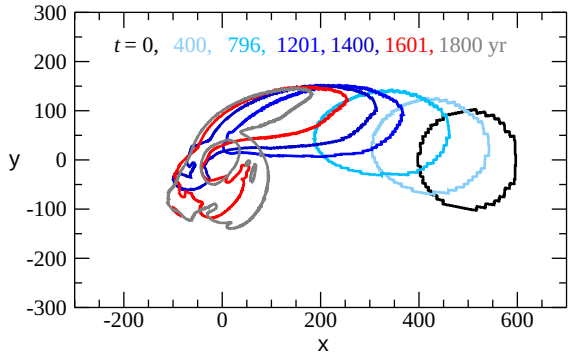


Figure 2. The evolution of the newly accreting cloudlet in model A. Each curve denotes the projection of the outer boundary of the accreting gas. The ordinate and abscissa denote $x = r\cos\varphi$ and $y = r\sin\varphi$, respectively. The epoch is shown by the same color on the top of the panel (Model A).

of the cloudlet projected on the $z = 0$ plane. We evaluated the cloudlet surface from the surface density of the cloudlet,

$$\Sigma_{\rm c}(x,y) = \int_{c>0} c(r,\varphi,z)\rho(r,\varphi,z)dz, \qquad (32)$$

where $(x, y) = (r\cos\varphi, r\sin\varphi)$. The tidal force of the protostar stretches the cloudlet in the direction of infall; the front side is accelerated more than the rear side. The cloudlet is confined by the warm gas and does not expand appreciably. At $t = 1498$ yr, the head of the cloudlet is compressed by the collision with the gas disk. The compression increases the number density up to 6.24×10^7 cm^{-3}. At $t = 1734$ yr, the disk is partly covered by the cloudlet. After the collision, the cloudlet changes its form; a part of it accretes on the disk while the rest leaves the protostar.

The upper panels of Figure 3 show the structure of the cloudlet and disk at $t = 1498$ yr. Figure 3a shows the gas of $c > 0$ (cloudlet) while Figure 3b does that of $c < 0$ (disk). The cloudlet is also bored by the disk to be separated into upper and lower halves. Above and below the disk surface, the cloudlet gas continues to infall, while the infall is blocked by the disk near the midplane. The inner edge of the cloudlet is shock compressed on the disk outer edge. On the other hand, the corresponding part of the disk is shaved to form an arm and accordingly the disk is highly asymmetric.

The lower panels of Figure 3 show the cloudlet and disk at $t = 1853$ yr. Main part of the former cloudlet covers a substantial fraction of the the disk and the other small fraction is scattered outward. The disk has several trailing arms in the outer region. The arms are shock waves induced by the impact of the collision with the cloudlet. The inner disk is also appreciably affected, though the details are subject to change. Note that the gravity is artificially softened in the region of $r <$ 50 au in our model and accordingly the gas motion is not reliable there.

Figure 2 shows the surface density distributions in the late stages. Most of the former cloudlet rotates around the protostar to accrete onto the disk, while a part of it forms an arm extending outward to be ejected. This ejection may be an artifact of our modeling in which we

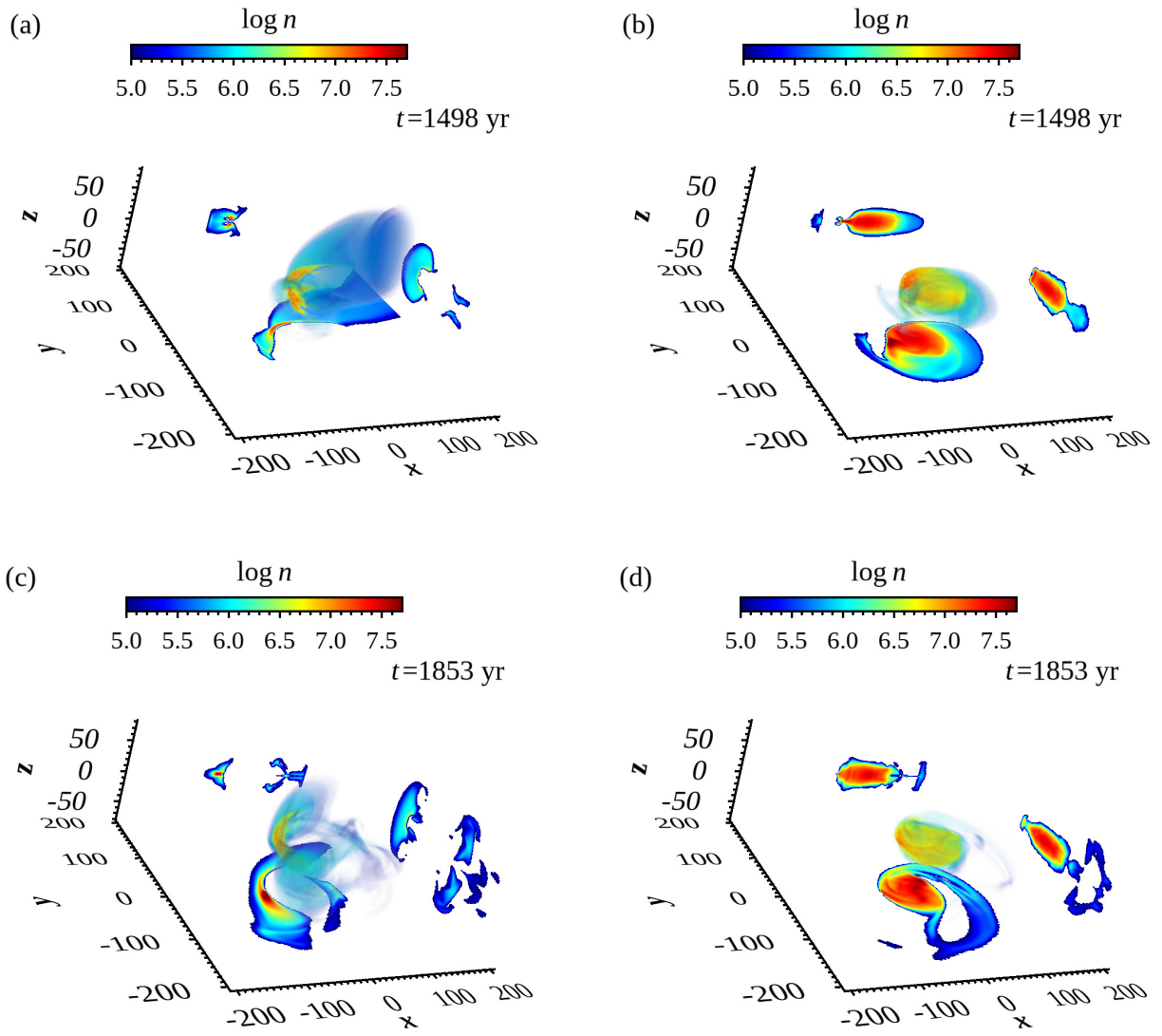


Figure 3. Panels a and c denote the distorted cloudlet in model A while panels b and d do the disk. The upper panels denote the stage at $t = 1498$ yr, while the lower ones do that at $t = 1853$ yr.

did not take account of angular momentum extraction by magnetic force or energy dissipation through radiation. However, it is plausible that a part of infalling gas is ejected from the protostar unless the energy dissipation is not efficient.

3.2. *Model A′*

Model A′ has the same initial condition as that of model A except for the initial distance of the cloudlet to the star. The initial distance is set to be $r_0 = 1000$ au while it is $r_0 = 500$ au in model A. The initial velocity of the cloudlet is reduced to 0.97 km s^{-1}. Figure 4 is the same as Figure 2 but for model A′. The cloudlet changes its form during the flight approaching to the star. The cloudlet has a fin-like structure on the side close to the star before the collision. The deformation is apparently larger on the rear side. The deformation is mainly due to the interaction with the warm gas, though it may be partly due to the tidal force. The head of the cloud is decelerated by the ram pressure, while the rear side is not.

Figure 5 shows the cloudlet and disk in model A′ at $t = 3784$ and 4202 yr. The notaion is the same as that of Figure 1. The left panel shows a stage before the collision, while the right panels shows and an early stage of the collision. The cloudlet collides with the disk around $t \simeq 3900$ yr. The delay of the collision is ascribed to the initial distance. As shown in Figure 5a, the cloudlet is deformed appreciably in model A′. But the difference is

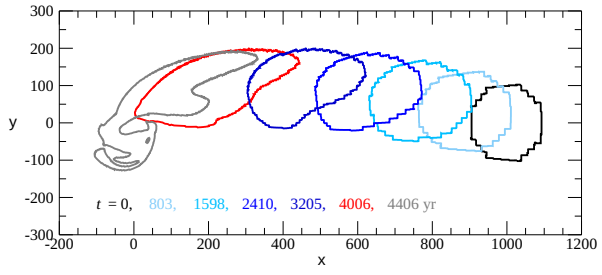


Figure 4. The evolution of the newly accreting cloudlet in model A′ (from 1,000 au away).

minor as seen from comparison between Figures 1b and 5b. The collision is so violent that it erases subtle differences in the cloudlet. We also note that our model of a cloudlet is highly ideal. A real cloudlet is unlikely to be a uniform sphere at any distance. Thus we conclude that the assumed initial distance of the cloudlet is not a critical parameter.

3.3. *Model B*

We assumed in models A and A′ that the orbital plane of the cloudlet coincides with that of the disk. However, a cloudlet may approach to the protostar from above the disk plane. We have constructed model B to examine the case in which the orbital plane of the cloudlet is inclined to the disk plane. The inclination angle is set to be $\psi_c = 30°$. The other model parameters are the same as those of model A.

Figure 6 is the same as Figure 1 but for model B at the initial stage ($t = 0$) and an early stage of collision ($t = 1311$ yr), while the enclosed animation shows the time evolution. The inclination of the orbit should not have a siginificant effect on the cloudlet before the collsion, since the warm gas is assumed to be spherically symmetric. The inclination changes the geometry of the collision. The cloudlet collides with the disk from the upper surface in model B, though it does from the outer edge in model A.

Figure 7 gives a zoom-in view of model B at $t = 1397$ yr and $t = 1860$ yr. The cloudlet is stretched by the tidal force to have a tail. The collision of the cloudlet induces a spiral wave in the disk. The impact is cleary seen in the left panel of Figure 7. At the same time, the density increases by the strike and a fraction of the disk is shaved. The cloudlet breaks the disk and goes through the disk midplane. The periastron of the cloulet is located under the midplane. The cloudlet gas returns to the upper side of disk after the passage of periastron. The right panel shows the collision of the cloudlet with the disk at a later stage.

Figure 8 shows the clouldlet and disk at $t = 1860$ yr separately while the enclosed animation shows the time evolution. Though the same stage is shown in the right panel of Figure 7, the viewing angle and coordinates are different. Figure 8 employs the Cartesian coordinates, (x', y', z), where

$$x' = x\cos 37.°5 + y\sin 37.°5, \quad (33)$$

$$y' = -x\sin 37.°5 + y\cos 37.°5, \quad (34)$$

to avoid degeneracy of the axes on the figure. Thus, the cross sections denote the gas distribution in the plane of $x' = 0$ and $y' = 0$. The viewing angle is specified by $i = 55°$, $\varphi_{\rm obs} = 50°$, and $\chi_{\rm obs} = 20°$. We use the same viewing angle in the Mock observation shown in §4. As shown in the panel, gas is ejected from the disk by the collision with the cloudlet.

3.4. *Models C and D*

We have constructed model C to examine the effects of the initial cloudlet size. The model parameters of Model C are the same as those of model B, except for the initial cloudlet size. The initial cloudlet radius is set to be $a_c = 200$ au in model C, while it is 100 au in model B. The mass of the cloudlet is 1.02×10^{-4} $M_\odot$ and is 8 times higher than that in models A and B.

Figure 9 shows two stages after the collision of the cloudlet with the disk in model C. The upper and lower panels show the stages at $t = 979$ and 1579 yr, respectively. The left panels denote the cloudlet by the voulme rendering and cross sections, while the right panels do the disk by the same manner. Since the cloudlet is larger, it reaches the disk a little earlier and occupies a larger volume. However, the collision forms a narrow arc of high density on the interface between the cloudlet and disk. The high density indicates the shock compression of the cloudlet. Since the arc is much narrower than the cloudlet, the width of the arm is irrelevant to the initial cloudlet size and related to the shock strength and cooling efficiency. Since the gas in the arc is compressed by the shock, the temperature should increase at once. In our model, the density is enhanced by a factor of $(\gamma + 1)/(\gamma - 1) = 41$ in the limit of strong shock.

Figure 9b displays that the disk has a slit corresponding to the arc. The disk outside the slit evolves into an arm at $t = 1579$ yr as shown in Figure 9d. The inner part of the disk is less affected by the collision. A significant fraction of the cloudlet is also not affected by the collision.

We have constructed model D to assess the effects of the cloudlet size on the deformation before the collision. The parameters of model D are the same as model C but for ψ_c. The orbit of cloudlet is coplanar to the disk

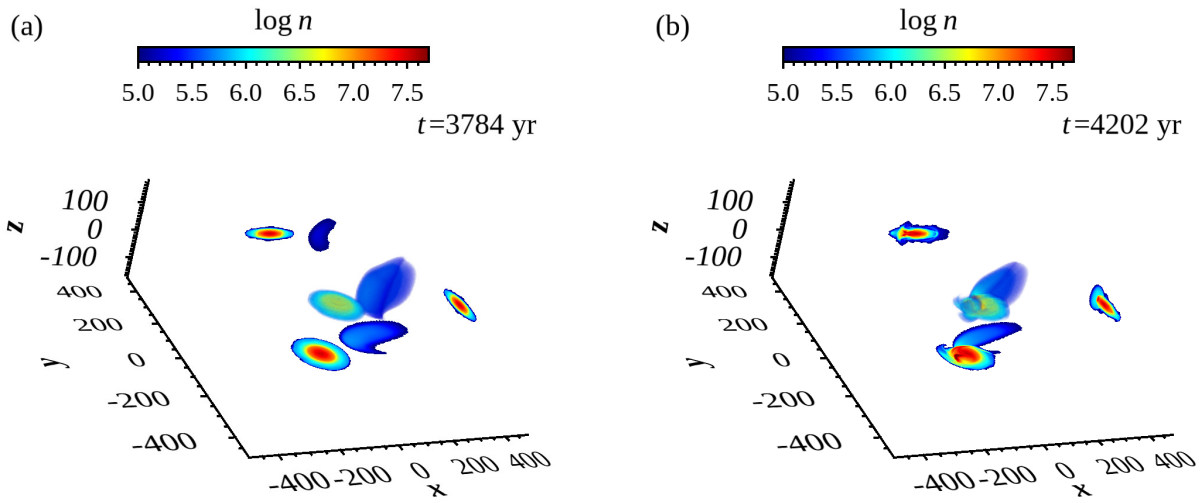


Figure 5. The same as Fig. 1 but for model A′ at $t = 3784$ yr and 4202 yr.

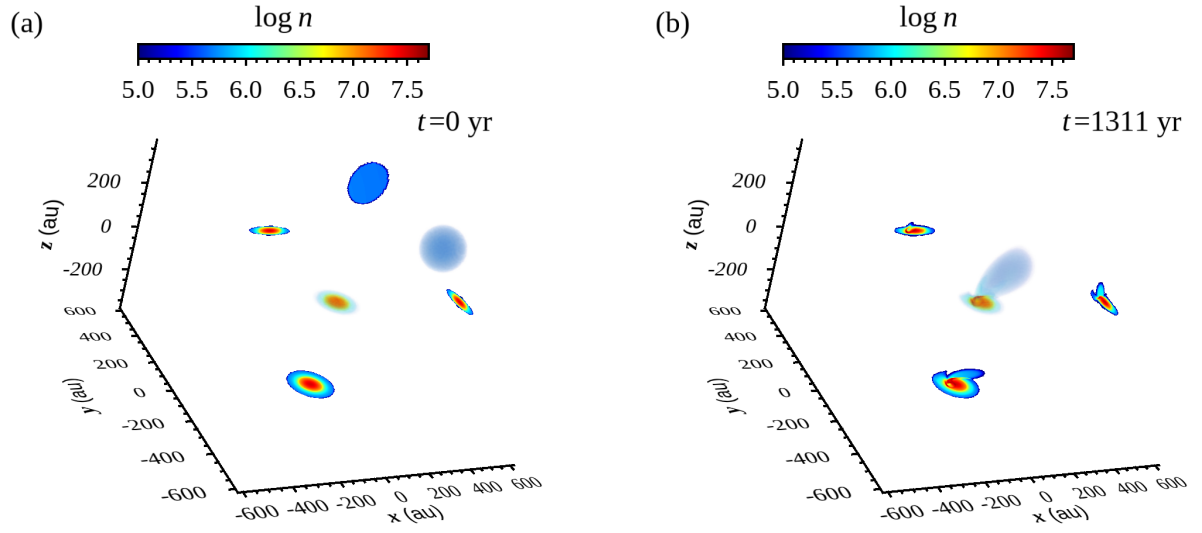


Figure 6. The left panel shows the initial gas distribution in model B while the right panel denotes that at $t = 1311$ yr. The animation shows the evolution of the density distribution in model B from $t = 0$ yr to 2831 yr.

in model D ($\psi_c = 0$) while it is inclined in model C. This difference is insignificant before the collision with disk. Note that the warm gas is spherically symmetric and the gas disk is disturbed little before the collision.

Figure 10 shows the shape of cloudlet projected on the plane of $z = 0$ in model D. The notation is the same as that of Figure 2. The cloudlet slims and changes its form from sphere to pear. The cloudlet has a trunk stretched toward the protostar before the collision. The deformation is due to the tidal force and warm neutral gas surrounding the cloudlet. Note that the pressure of the warm neutral gas is higher at a shorter distance from the protostar. The high pressure compresses the cloudlet when it approaches to the protostar. The cloudlet changes from a sphere to a pear-like shape before the collision also in model C. So, the cloudlet gives an impact of small scale on the disk even when it is initially as large as the disk.

The cloudlet begins to cover the whole disk around $t \simeq 1400$ yr in model D, though the major part of the cloudlet is still approaching to the protostar. The cloudlet turns around the protostar while disturbing the disk. Around $t \simeq 2000$ yr, the cloudlet gas approaching to the protostar is comparable with that leaving.

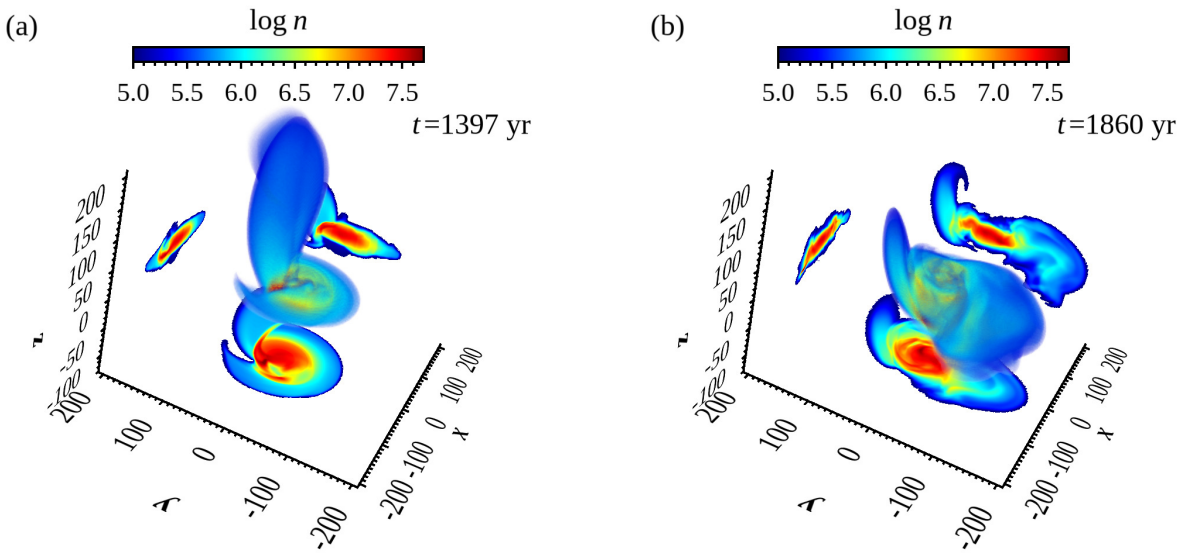


Figure 7. The gas distribution around the protostar in model B at $t = 1397$ yr (left) and 1860 yr (right).

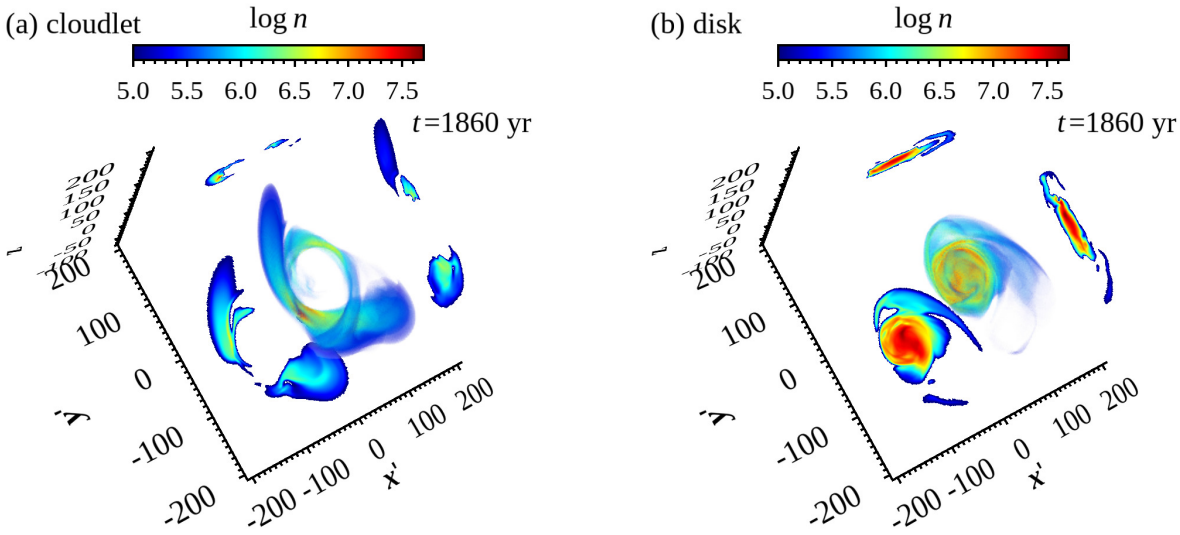


Figure 8. The left and right panels denote the cloudlet and disk gases in model B at $t = 1860$ yr, respectively. The same stage is shown in the right panel of Fig. 7 but from a different viewing angle. The animation shows the time evolution up to $t = 2381$ yr.

4. COMPARISON WITH OBSERVATION

In this section we compare our model with the observation of TMC-1A. Figure 11 shows the line emission of CS (J = 5-4; 244.9355565 GHz $E_{\rm u}$ = 35 K) and SO ($J_N = 7_6 - 6_5$ 261.8437210 GHz, E_u =48 K) by the channel maps. The data were taken by ALMA (ADS/JAO.ALMA#2013.0.01102.S, PI:N.Sakai), which were analyzed and reported by Sakai et al. (2016). The beam size is $0.''69 \times 0.''40$ (PA = 11°) and accordingly 97 au × 56 au on the sky plane at the distance of 141 ± 7 pc (Zucker et al. 2019). The beam size and linear scale are shown in the upper left channel map of $V = 2.36$ km s^{-1}. Each channel map covers the area of $\Delta\alpha = 6.''87$ in the right ascension and $\Delta\delta = 7.''00$ in the declination. The crosses denote the continuum peak, $(\alpha_{2000}, \delta_{2000}) = (04^{\rm h}39^{\rm m}35.2, 25°41'44.''19$. The color denotes the intensity of CS while the contours do that of SO. The color scale is given in the right bottom corner, while the contour denote $I_\nu = 50$, 100, 150, 200, and 250 mJy beam^{-1}. We assume the systemic velocity of TMC-1A to be 6.36 km s^{-1} according to the channel maps, which is slightly lower than the reported

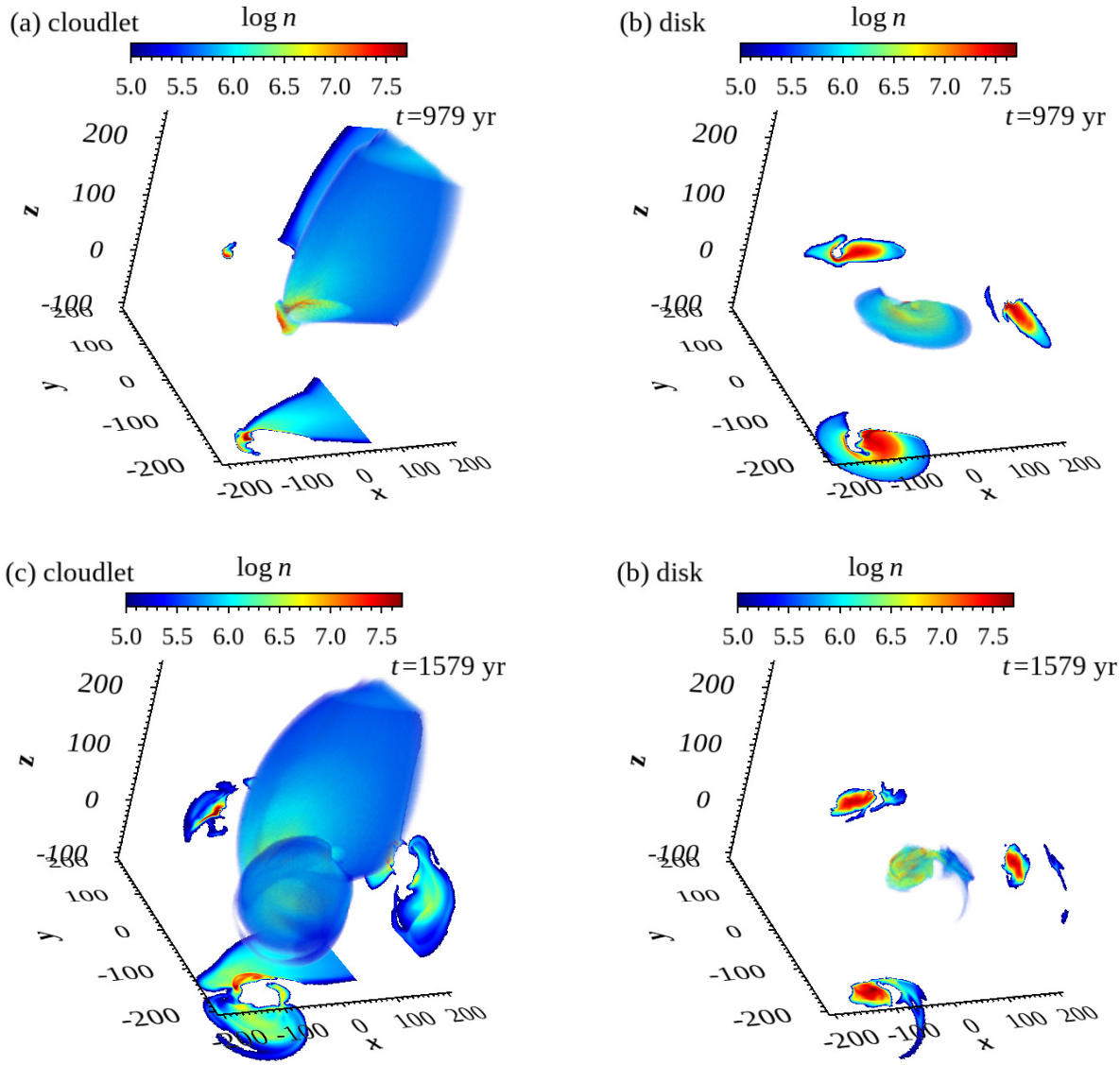


Figure 9. Early stage of the collision in model C. Panels (a) and (c) denote the cloudlet, while panels (b) and (d) do the disk.

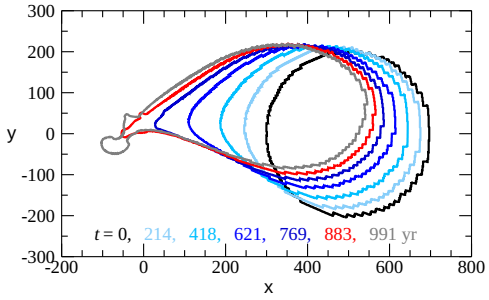


Figure 10. The same as Fig. 2 but for model D

value, 6.6 km s^{-1}, (Yen et al. 2013; Harsono et al. 2014) although the difference ($\sim$ 0.24 km s^{-1}) is comparable to the thermal linewidth. The blue-shifted emission is much stronger than the red-shifted one (See also figures 1b and 1c of Sakai et al. 2016). The CS emission has a strong peak in the region north-east to the protostar. We find diffuse emission in the channel maps of $V = 5.56$ and 5.96 km s^{-1}, while not in those of $V = 6.36$ and 6.76 km s^{-1}.

The SO emission is strong in the region south of the protostar. This region corresponds to the impact of the cloudlet to the disk in our model, as mentioned in §§3.1 and 3.4. This feature of the SO emission is similar to the DG Tau and HL Tau cases observed by Garufi et al. (2022). The foot point of the streamer on the disk is bright in DG Tau and HL Tau. The line of sight velocity matches with the estimate based on the kinematical model.

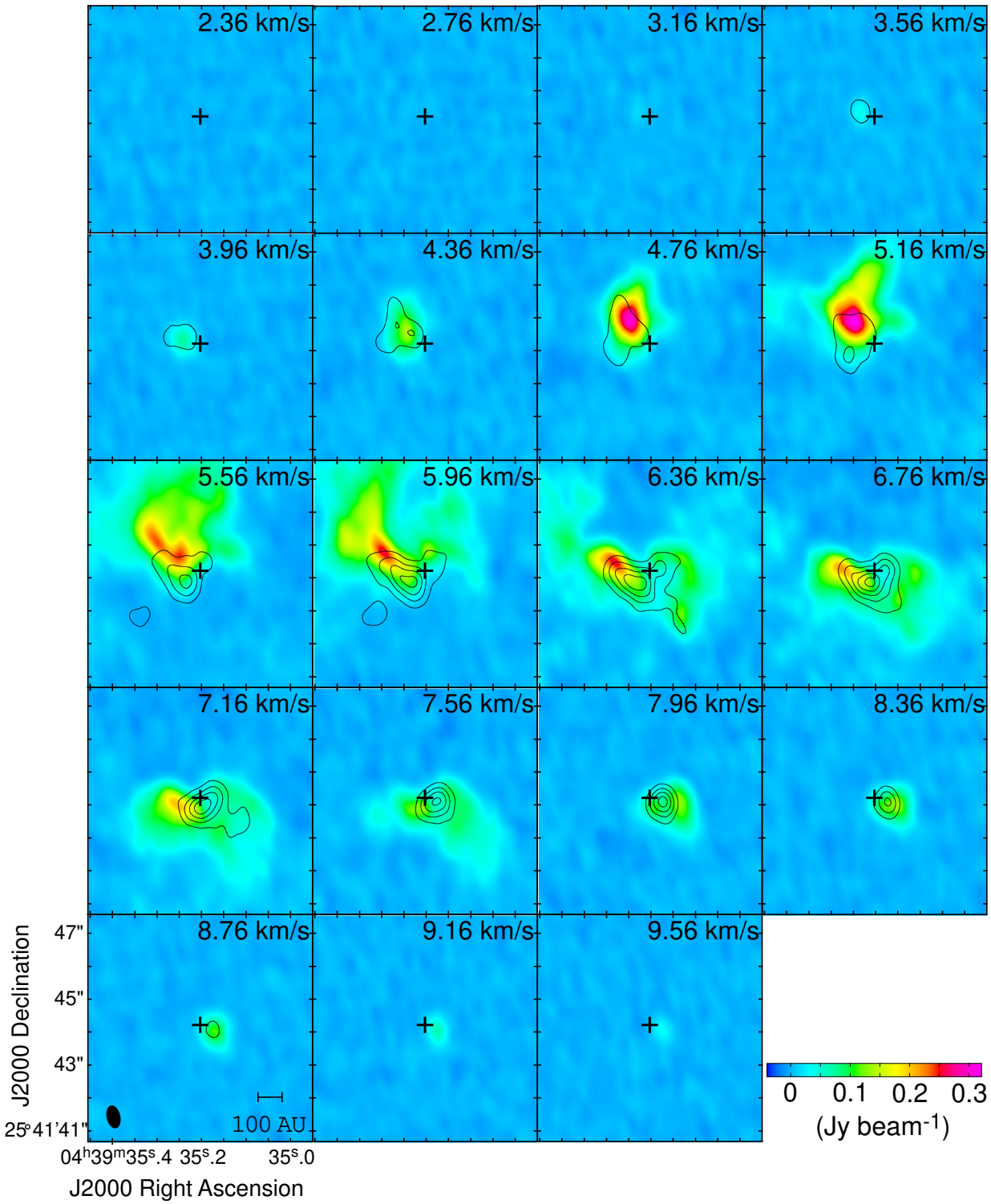


Figure 11. Velocity channel maps of the CS J=5-4 line taken by ADS/JAO.ALMA#2013.0.01102.S (see details in Sakai et al. 2016). The lowest contour and the contour interval are 50 mJy. The cross marks represent the position of the continuum peak.

Model C reproduces the observed features qualitatively. Figure 12 is mock channel maps made based on the pseudo observation of model C at $t = 1860$ yr. Each panel shows the area 963 au $\times$ 987 au on the sky, which corresponds to $6.''8 \times 7.''0$ at the distance of 141 pc. The color denotes the column density along the line of sight in the specified range of the line of sight velocity. The inclination angle is assumed to be $i = 55°$ ($0°$ for face-on, Harsono et al. 2014). The viewing angle is specified by $\varphi_{\rm obs} = 355°$ and $\chi_{\rm obs} = 60°$. Since the CS emission traces mainly the newly accreted gas seen in L1527 (Sakai et al. 2014a,b), we assume that only the gas of $c > 0$ (i.e., the cloudlet) contains CS in making the channel map. The mock channel maps show an arc in the range of 3.96 km s^{-1} $\leq V \leq$ 4.76 km s^{-1}. This corresponds to the former cloudlet gas compressed by the collision with the disk.

Model A cannot reproduce the observed features. Figure 13 is the same as Figure 12 but for model A at $t = 1853$ yr. The emission appears in the channel maps of 3.16 km s^{-1} $\leq V \leq$ 3.96 km s^{-1}, though the observation does not show such highly blue-shifted emission.

The main difference of model B from model A is the orbital plane of the cloudlet. While the cloudlet has nearly the same velocity in both the models, the line of sight velocity depends on the viewing angle in model C. The orbit of cloudlet is inclined by $85°$ for the viewing angle of Figure 12, while it is inclined by $55°$ irrespectively of the viewing angle in model A. Note that the Keplerian rotation velocity is 3.07 km s^{-1} at $r = 50$ au. The cloudlet should have a velocity of ~ 4.4 km s^{-1} at $r = 50$ au if it follows the parabolic orbit. We can reconcile this high velocity with the observed relatively low blue-shift only when the orbit is significantly inclined to the disk. The line of sight velocity is reduced by the projection. Since the orbit is close to face-on in model C, the line of sight velocity is low. Model B cannot reproduce the spatial extent of blue-shifted emission, though the amount of the Doppler shift can be adjusted by the inclination of the cloudlet orbit.

Aso et al. (2015) measured the infall velocity from the C^{18}O (J = 2-1) emission taken with ALMA. The measured infall velocity is only 30 % of that expected from their free-fall model in which the orbital plane of the infalling gas coincides with the disk. Though they ascribed the low infall velocity to deceleration by magnetic force, it may be due to the geometrical effect. If the C^{18}O emitting gas is coplanar with the cloudlet of model C, the line of sight velocity is much lower than that expected for it to be coplanar with the disk.

If IRAS 04365+2535, the protostar in TMC-1A, were a close binary, it could be a source of asymmetry. The SO emission might be associated with a component of the binary. However, we need another explanation for the blue-asymmetry of the CS emission for this case. The localization of the CS emission around the protostar indicates that the gas accretion is on a short timescale. If the accretion were continuous, the molecular emission should be more extended. The asymmetry suggests that the gas infall dominates over the rotation. If the rotation were dominant, the asymmetry should be erased out by differential rotation. The localization and asymmetry favor temporal and asymmetric gas accretion such as clouldlet capture.

The arc-lie features seen in the channel maps of $v =$ 4.36 and 4.76 km s^{-1} may correspond to the spiral-like feature discovered by Aso et al. (2021). They observed TMC-1A with SMA and ALMA at $\lambda = 1, 3$ =mm and discovered a spiral-like feature in the continuum emission. They derived the spiral by subtracting component symmetric around the star from the high resolution image of the disk. The residual after the subtraction appears in in the East side of the disk and is associated with the blue-shifted C^{18}O emission in the range ($v = 4.35 - -5.15$ km s^{-1}). See Figure 7 of Aso et al. (2021) where the channel map of C^{18}O is overlaid on the residual intensity.

Sakai et al. (2016) noticed another asymmetry in the line emission of SO ($J_N = 7_6$-6_5). The SO line, which could be used to a shock tracer, is found to be stronger in south-west to west part of the protoostar (Figure 1 of Sakai et al. 2016). This component is also seen in the red shifted components of the CS map (7.56-9.16km s^{-1}), which is also consistent with model C. Panel (c) of Figure 3 and the right panel of Figure 8 show the disk at at $t = 1853$ yr in model A and that at $t = 1860$ yr, respectively. Both the disks have a partial loss in the northern side of the disk. The loss formed by the collision with the cloudlet rotates faster than the cloidlet. The disk rotation assimilates the loss and is weaker in model B than in model A.

5. DISCUSSIONS

So far, the physical structure of the disk/envelope system of TMC-1A has been discussed by using observations of a single molecule at a time. For instance, Aso et al. (2015) analyzed the C^{18}O data by a combination of the Keplerian model and the infalling model, while Sakai et al. (2016) analyzed the CS data by the infalling rotating envelope model (Sakai et al. 2014a; Oya et al. 2014). Sakai et al. (2016) also pointed out the weak shock feature around the centrifugal barrier of the infalling rotating envelope. These results gave important information on local physical processes in the complex

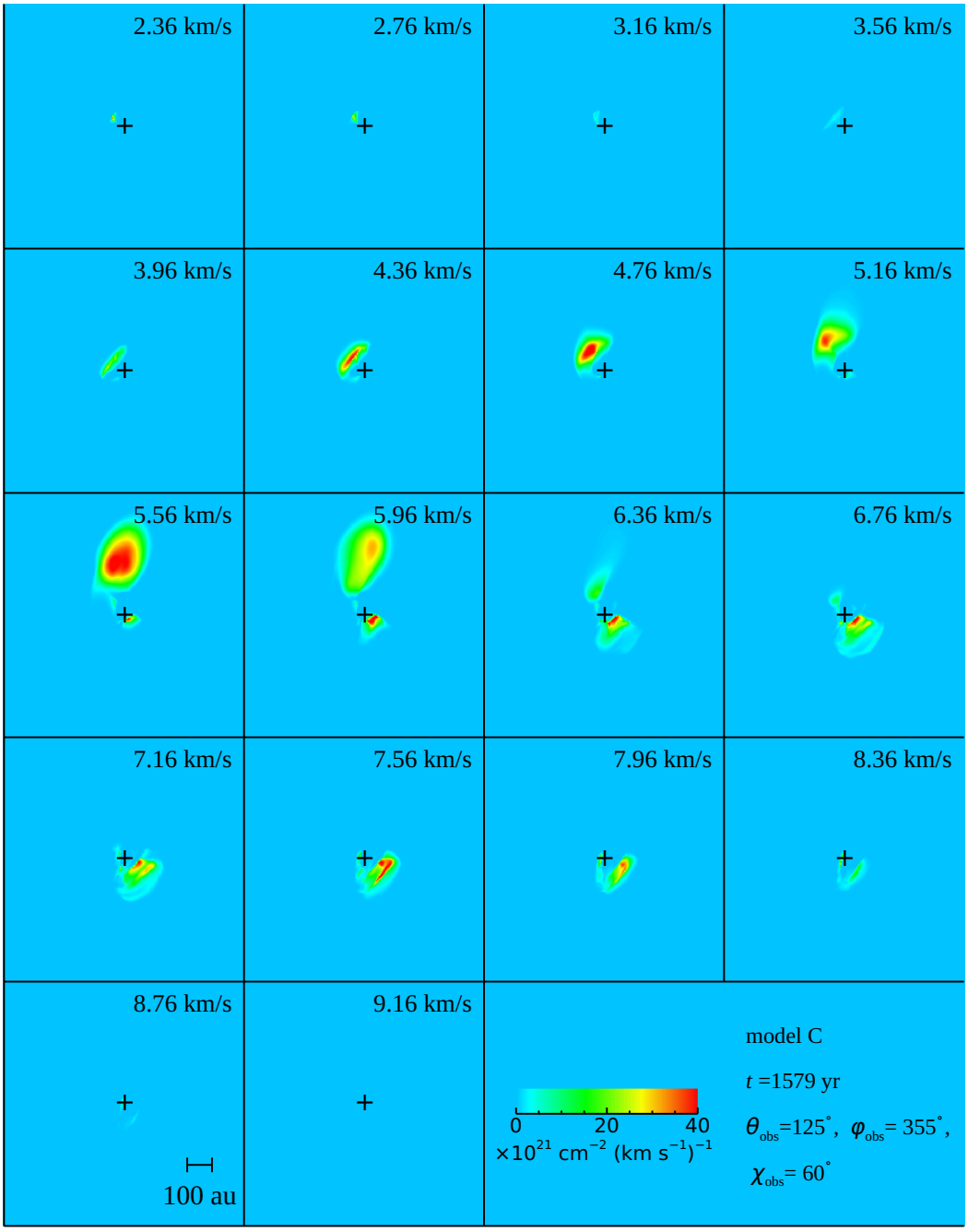


Figure 12. Mock channel maps of model C at $t = 1860$ yr. The color denotes the density integrated over the line of sight, i.e., $\Sigma(X, Y, V)$ given by Eq. (28). The observer's line of sight is specifed by $\theta_{\rm obs} = 125^\circ$ ($i = 55^\circ$), $\varphi_{\rm obs} = 355^\circ$, and $\chi_{\rm obs} = 60^\circ$. The line of sight velocity increases from the top left $V = 4.50$ km s^{-1} to the right bottom 8.36 km s^{-1}, where the systemic velocity is assumed to be 6.40 km s^{-1}.

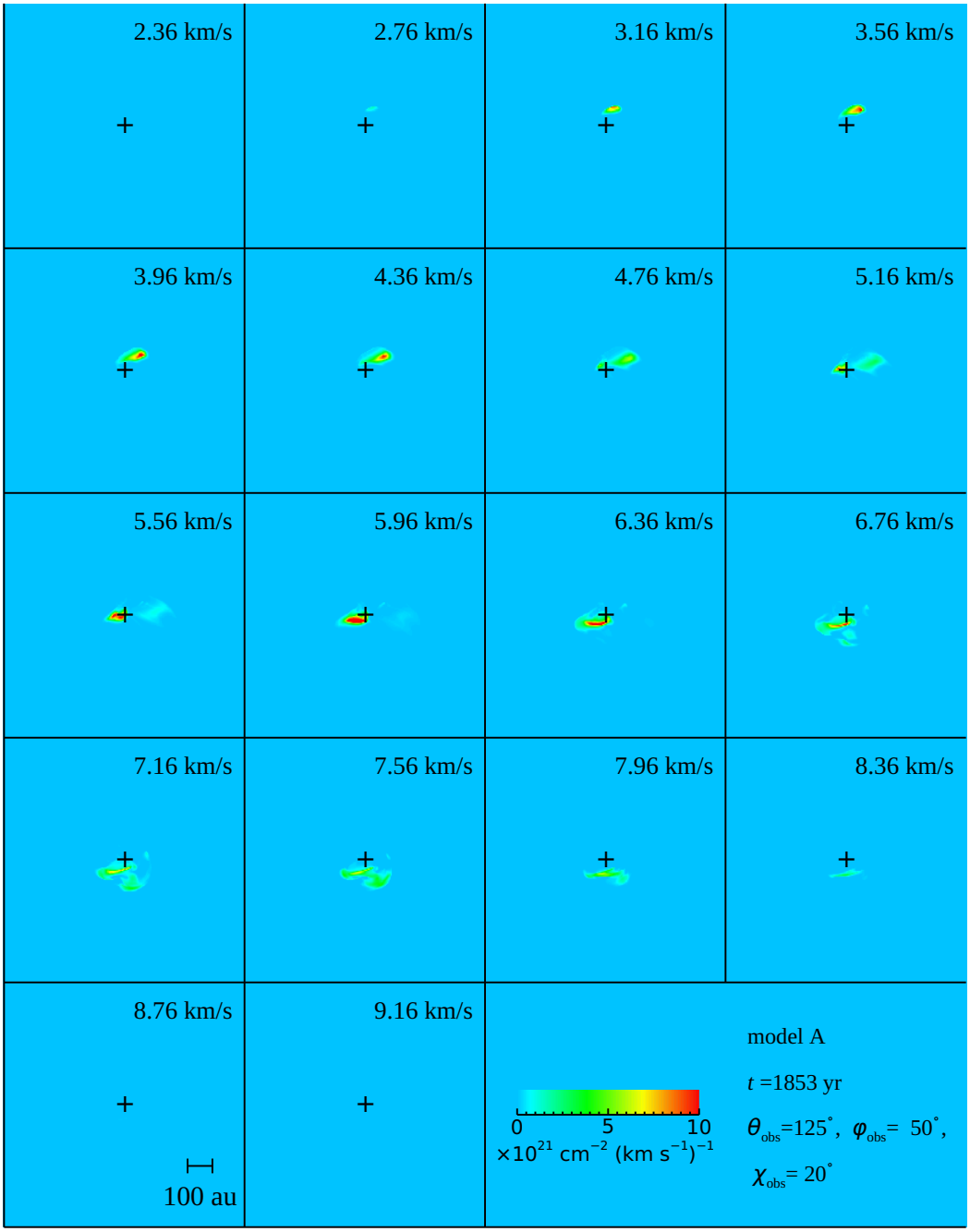


Figure 13. The same as Fig. 12 but for model A at $t = 1853$ yr. The viewing angle is given by $\theta_{\rm obs} = 125^\circ$ ($i = 55^\circ$), $\varphi_{\rm obs} = 50^\circ$ and $\chi_{\rm obs} = 20^\circ$

disk/envelope system, but their origins and mutual relations have not been clarified under a broader picture. As shown in the previous sections, our cloudlet capture model can reasonably explain overall features observed in line emissions of CS, $C^{18}O$, and SO. It validates the picture presented by Sakai et al. (2016). A cloudlet reaches the centrifugal barrier and a part of it recedes from the protostar again. Since the orbit of the receding gas does not intersect with the approaching gas, the infall continues unless the pre-existing disk is a serious obstacle. A cloudlet transforms into an arc or a stream during the infall as shown in Figure 9. Both the head and tail are confined in narrow areas while they have different velocities. Thus, it can explain why the line emission is confined in a narrow area in each channel map. The collision of a cloudlet with disk can also explain the asymmetric SO bright spot in the observation. Furthermore, it can explain relatively slow line of sight velocity if the orbit of cloudlet is nearly face-on.

As stated in §1, high asymmetry is seen in some young protostars even when they are not close binaries. Their asymmetries may also be explained by a cloudlet capture. The asymmetric gas distribution around the disk/envelope system is often seen in low-mass protostellar sources. For instance, Yen et al. (2014) observed the Class I protostar L1489 IRS in the CO and its isotopologue lines with ALMA and revealed the red-shifted gas falling to the red-shifted edge of the large Keplerian disk. Since the corresponding structure is not seen in the blue-shited side, this feature can be regarded as an asymmetric accretion. More recently, Pineda et al. (2020) studied the Class 0 protostar Per-emb-2, which is a close binary system with separation of 20 au, in the HC_3N lines with NOEMA. They found an elongated gas clump with the size of 10500 au streaming to the protostar from one side. This feature is quite similar to the case of TMC-1A.

Very recently, Garufi et al. (2022) have reported streamers in DG Tau and HL Tau. The streamers are visible in the CO and CS emission lines in DG Tau, while in HCO^+ and CS emission lines in HL Tau. They have also detected SO and SO_2 line emission from the foot point of the streamer on the disk. Since SO and SO_2 are good tracers of a shock, the emission is an evidence that the streamer is a trail of infalling gas. They confirmed the infalling gas scenario by an analytic streamline model. Interestingly, they argue that the southern streamer is continuation of the northern one and hence an outflow in DG Tau (see Fig. 7 of Garufi et al. 2022). Their interpretation supports our model that the red-shifted component is continuation of the blue-shifted one in TMC-1A.

Though we ignored the magnetic field in our modeling for simplicity, the cloudlet may be permeated by magnetic field. If the magnetic field is strong enough, it should decelerate the infall of the cloudlet appreciably as suggested by Aso et al. (2015). However, Garufi et al. (2022) have succeeded in reproducing the streamers in DG Tau and HL Tau by taking account of the gravity only. This means that the magnetic field is weak in DG Tau and HL Tau. It seems reasonable to assume that the magnetic field is also weak in TMC-1A. Weak magnetic field may play a role in late evolution. Gas ejection seen in our simulations would be changed, if initially weak magnetic field were taken into account. Unno et al. (2022) have shown that initially weak magnetic field is amplified by the collision of cloudlet. When the cloudlet is larger than the disk thickness, the amplified magnetic field accelerate and eject a part of the cloudlet from the system.

The asymmetric feature is also seen around some other Class II sources. Huang et al. (2021) observed the CO (2-1) emission toward GM Aur with ALMA and found the blue-shifted gas extending from the disk on a 1000 au scale. They interpret it as the remnant gas of the envelope or the cloud component infalling to the disk. They also point out that the nearby Class II sources, SU Aur and AB Aur, would have a similar asymmetric feature, on the basis of the Herschel SPIRE data. Above all, the asymmetric feature seems more or less frequent occurrence in young sources.

It is interesting to examine the possibility that gas accretion onto a protostar is mainly through cloudlet capture. If it is the case, the accretion rate is highly variable in nature. The capture of cloudlet can change the disk rotation axis which is parallel to the total angular momentum of the disk. Each cloudlet should have a different angular momentum vector and the capture should change the direction. The change may result in launch of multiple outflows in IRAS 15398-3359 observed by Okoda et al. (2021). Some cloudlets may recede from the protostar before reaching a close vicinity of it.

It should be noted that existence of a warm gas is a key issue in our cloudlet capture model. As mentioned by Dullemond et al. (2019); Küffmeier et al. (2019); Küffmeier et al. (2021), an isothermal cloudlet expands and disperses if it is not confined by pressure. A theory of protoplanetary disk also invokes a surrounding warm tenuous gas (see, e.g., Dutrey et al. 2014). The disk surface should also be in pressure equilibrium with the warm gas. Then,the cloudlet and disk surface have nearly the same density since they have the same pressure and nearly the same temperature. If the density of the cloudlet is nearly the same as that of the disk,

the impact of the cloudlet collision should be significant since the ram pressure exceeds the gas pressure of the disk. The disturbance by the collision will induce shock heating and mixing of disk gas, both of which will affect the chemical evolution of the disk.

We point out that the inclination of the orbital plane of the cloudlet to the disk may enhance the shock strength. When the cloudlet is coplaner, the radial velocity vanishes at the centrifugal barrier. The slow radial velocity may cause a weak shock. However, the cloudlet has a still large azimuthal velocity. If the orbital plane is inclined, a fraction of it results in a relative velocity with the disk. Since the rotation velocity reaches several km s^{-1}, a fraction of it is still supersonic and will contribute to the shock.

TH thanks Yosuke Matsumoto for his contribution on the visualization of our numerical simulations. We thank an anonymous reviewer for their constructive comments. This work was supported by JSPS KAKENHI Grant Numbers JP18H05222, JP19K03906, JP20H05845, JP20H05847, JP20H00182. This study used the ALMA data set ADS/JAO.ALMA#2013.0.01102.S. ALMA is a partnership of the European Southern Observatory, the National Science Foundation (USA), the National Institutes of Natural Science (Japan), the National Research Council (Canada), the NSC and ASIAA (Taiwan), and KASI (Republic of Korea), in cooperation with Republic of Chile. The Joint ALMA Observatory is operated by ESO, the AUI/ NRAO, and NAOJ.

Facility: ALMA

REFERENCES

Andrews, S.M., Huang, J., Pérez, L.M., et al. 2018, ApJL, 869, L41

Artur de la Villarmois, E., Jørgensen, J.K., Kristensen, L.E. et al. 2019, A&A, 626, A71

Aso, Y., Ohashi, N., Saigo, K. et al. 2015, ApJ, 812, 27

Aso, Y., Kwon, W., Hirano, N. et al. 2021, ApJ, 920, 71

Bjerkeli, P., Matthijs, H.D., van der Wiel et al. 2016, Nature, 540, 406

Dutrey, A., Semenov, D., Chapillon, U. et al 2014 Protostars and Planets VI ed H. Beuther et al (Tuscon, AZ: Univ. Arizona Press) 317

Dullemond, C.P., Küffmeier, M., Goicovic, F., et al. 2019, A&A, 628, A20

Fukagawa, M., Hayashi, M., Tamura, M. et al. 2004, ApJL, L53

Garufi, A., Podio, L. Codella, C. et al. 2022, A&A, 658, A104

Hanawa, T., & Matsumoto, Y. 2021, ApJ, 907,43

Harsono, D., Jørgensen,J.K., van Dishoeck, E.F. et al. 2014, A&A, 562, 77

Harsono, D., van der Wiel, M.H.D., Bjerkeli, P. et al. 2021, A&A, 646, A72

Hartmann L. and Kenyon S. J. 1996, ARA&A, 34 207

Hennebelle, P., and Falgarone, E. 2012, A&A Rv, 20, 55

Huang, J., Bergin, Öberg, K. et al. 2021, ApJS, 257, 19

Imai, M., Oya, Y., Sakai, N. et al. 2019, ApJL, 873, L21

Küffmeier, M., Haugbølle, T. and Nordlund, Å 2017, ApJ, 846, 7

Küffmeier, M., Goicovic, F., & Dullemond, C.P. 2019, A&A, 663, A3

Küffmeier, M., Dullemond, C.P., Reissl, S., Goikovic, F.G. 2021, A&A, 656, A161

Miranda, R., Lai, D., Méheut, H. 2016, MNRAS, 457, 1944

Nakatani, R., Liu, H.B., Ohashi, S. et al. 2020, ApJL, 895, L2

Okoda, Y., Oya, Y., Logan, F. et al. 2021, ApJ, 910, 11

Oya, Y., Sakai, N., Sakai, T., et al. 2014, ApJ, 795, 152

Oya, Y., Sakai, N., Watanabe, Y. et al. 2016, ApJ, 837, 174

Pineda, J.E., Segura-Cox, D., Casselli, P. et al. 2020, NatAs, 4, 1158

Sakai, N., Sakai, T., Hirota, T. et al. 2014a, Nature, 507, 78

Sakai, N., Oya, Y., Sakai, T. et al. 2014b, ApJL, 791, L38

Sakai, N., Oya, Y., Lópezz Sepulcre, A. et al. 2016, ApJL, 820, L34

Sakai, N. Hanawa, T., Zhang, Y., et al. 2019, Nature, 565, 206

Unno, M., Hanawa, T., Takasao, S. 2022, private communication, (submitted to ApJ).

Yen, H.-W., Takakuwa, S., Ohashi, N., Ho, P.T.P. 2013, ApJ, 772, 22

Yen, H.-W., Takakuwa, S., Ohashi, N. et al. 2014, ApJ, 793, 1

Zucker, C., Speagle, J.S., Schlafly, E.F. et al. 2019, ApJ, 879, 125